Microstructure, mechanical properties and cracking behaviour in a gamma'-precipitation strengthened nickel-base superalloy fabricated by electron beam melting

Peng, H., Shi, Y., Gong, S., Guo, H. & Chen, B.

DOI 10.1016/j.matdes.2018.08.054
ISSN 0261-3069
ESSN 0264-1275

Publisher: Elsevier

Microstructure, mechanical properties and cracking behaviour in a γ'-precipitation strengthened nickel-base superalloy fabricated by electron beam melting

H. Peng[a,b], Y. Shi[b], S. Gong[a,b], H. Guo[a,b], B. Chen[c,*]

[a]*Key Laboratory of High-Temperature Structural Materials & Coatings Technology, Ministry of Industry and Information Technology, Beihang University, 37 Xueyuan Road, Beijing 100191, China*

[b]*School of Materials Science and Engineering, Beihang University, 37 Xueyuan Road, Beijing 100191, China*

[c]*The Institute for Advanced Manufacturing and Engineering, Faculty of Engineering, Environment and Computing, Coventry University, Beresford Avenue, Coventry CV6 5LZ, UK*

[*]Corresponding authors. E-mail addresses: ac0955@coventry.ac.uk

Abstract

The influences of EBM processing and post-processing on microstructure, mechanical properties and cracking behaviour in a γ' precipitation-strengthened nickel-base superalloy DZ125 are critically assessed. Results show that a solution treating and ageing (STA) is required to obtain γ' precipitates with a cuboidal shape. The columnar grain width was found to gradually increase from the bottom to the top of the as-EBM sample having a total build height of 80 mm, whereas there was little gradient in γ' size. The presence of EBM induced intergranular cracks can be closed by hot isostatic pressing (HIP), however reappearance of intergranular cracks with a much wider crack opening width was observed after STA treatment. EBM induced cracks are classified as liquid-state cracking, as the classic dendritic morphology were found on the cracked surfaces. The post-processing induced cracks can be attributed to the effect of γ' dissolution and re-precipitation of fine γ' during the cooling stage of solution treatment. The results suggest that HIP is not an effective approach in healing liquid-state cracks in EBM fabricated γ' precipitation-strengthened superalloys.

Keywords: Microstructure; Mechanical properties; Cracking; Electron beam melting; Nickel-base superalloys

1. Introduction

The outstanding mechanical properties of nickel-base superalloys particularly at elevated temperatures are related to the diversity of alloy elements and the dual-phase microstructure that consists of ~70 vol% cuboidal coherent γ' precipitates [1]. Many nickel-base superalloys with carbon content up to 0.2 wt% can form various types of carbides, depending on the specific alloy composition, processing route and service history. The presence of these precipitates would further enhance the creep resistance of superalloys by providing a mechanical pinning of grain boundaries [2]. For example, it has been reported in [3-5] that Hf-rich MC carbides do not provide an easy path for rapid crack propagation and hence further improve the creep resistance.

Electron beam melting (EBM) is a powder-bed additive manufacturing (AM) process. In contrast to selective laser melting (SLM), the electron beam works under vacuum conditions and can be moved at extremely high velocities with a high power, more importantly, a high build temperature is available with EBM [6]. In addition, the EBM process-inherent rapid and directed solidification leads to very fine microstructures. The same material processed with different EBM parameters can either be texture-free or highly-textured [7, 8], and fine or coarse-grained [9, 10]. This offers a great potential to design engineering components where the local material properties can be tailored. In general, the obtained mechanical properties in a nearly 100% dense AM materials are comparable to, if not better than, those associated with conventional processes such as casting and forging [11-14].

Nickel-base superalloys can be roughly divided into weldable and non-weldable groups [15]. The latter are highly susceptible to cracking due to γ' precipitation. Thus non-weldable superalloys are difficult to be processed by AM; it is essentially a welding process. In terms of the weldable group, Inconel 718, as a most widely used γ'/γ" precipitation-strengthened nickel-base superalloy, have been successfully processed by EBM [7, 8, 14, 16, 17] and SLM [11, 18, 19]. The presence of EBM induced pores in Inconel 718 were reported in [14]. The Inconel 718 work by Kirka et al. [17] showed that such pores can be easily closed by hot isostatic pressing (HIP). Like the EBM process, the presence of SLM induced pores in Inconel 718 can be removed by HIP [18, 19].

In terms of the non-weldable group, tensile yield strength of SLM-built Hf-rich

CM247LC was found to be comparable with that of cast alloy [12, 20]. However, the formation of cracks remains as a challenge for SLM. Cloots et al. [21] studied SLM-built Inconel 738LC and results showed that a reduction in the crack density can only be achieved with increasing porosity. Harrison et al. [22] claimed that the high crack susceptibility in SLM-built Hastelloy-X alloy can be reduced significantly by increasing the substitutional elements. However, this approach would only apply to the solid solution-strengthened nickel-base superalloys, i.e. Hastelloy-X belongs to the weldable group [15].

Recent work [13, 23] has demonstrated that EBM is a particularly promising approach to fabricate defect-free and complex parts made of γ' precipitation-strengthened CMSX-4 and Rene 142 superalloys. The resulting microstructure of CMSX-4 in as-EBM condition was found to be about two orders of magnitude smaller than that processed by casting [23]. Murr et al. [13] commented that there was some evidence for cracking within columnar grains in EBM-built Rene 142 although they did not show any crack features. In addition, Ruttert et al. [24] reported that the presence of intergranular cracks in as-EBM CMSX-4 was difficult to be closed by HIP. More recently, the presence of intergranular cracks was also found in an unspecified type of non-weldable superalloy fabricated by EBM [25].

The aim of this work is to critically assess the influences of EBM parameters and post-processing on microstructure, mechanical properties and cracking behaviour in a γ' precipitation-strengthened superalloy, DZ125. The post-processing included both HIP and solution treating and γ' precipitation ageing (STA). A particular emphasize of this work it to examine the crack formation mechanism and provide important insights on whether HIP is an effective approach in healing EBM induced cracks. DZ125 is a Chinese commercial columnar-grained, γ' precipitation-strengthened nickel-base superalloy that is similar to Rene 142 [13] and CM247LC [12] in terms of Al, Ti (γ' forming elements) and Hf contents.

2. Experimental

2.1. EBM fabrication

Arcam A2XX machine with Control Software 3.2 was used for EBM fabrication in

a manual mode. There are many EBM processing parameters which can be varied to create different microstructures as described in [7, 8]. Experiments consisting of EBM building 9 rectangle samples (25 × 25 × 80 mm^3) per batch were carried out with in total 6 parameter sets, Table 1. All these parameter sets are within the stable EBM processing window because the whole build process did not show any metal ball formation, smoke and powder splashing phenomena. Area energy E_A is a function of beam power P, scanning speed v, and line offset L_{off}. These three EBM parameters were changed in such a way that area energy E_A varied from 1.88 J/mm^2 to 5.00 J/mm^2, Table 1. According to [7], E_A can be expressed:

$$E_A = \frac{P}{vL_{off}} \tag{1}$$

v varied from 800 mm/s to 3200 mm/s, L_{off} ranged from 0.02 mm to 0.15 mm, and P was either 600 W or 300 W, Table 1.

Fig. 1(a) shows a schematic diagram of one batch of as-EBM samples. A 10 mm thick stainless steel plate with a surface area of 110 × 110 mm^2 and a pre-heat area of 100 × 100 mm^2 was used as starting plate. No supports were applied for the EBM fabrication. The plate was then heated by the electron beam to a pre-defined build temperature of 1050 °C[1] when a vacuum pressure of 2×10^{-3} mbar within the chamber was reached. The build temperature was measured using a thermocouple connected to the bottom of the plate. A 50 μm thick layer of pre-alloyed powders was raked onto the plate prior to pre-heating. This was followed by contour melting and hatch melting. This procedure was repeated layer-by-layer. The samples were fabricated by a line order EBM scanning strategy, where the electron beam scans in a snake-like way with a specific line offset L_{off}, Fig. 1(b). The hatch melting direction was changed by 90° after each build layer. The total fabrication time per batch was between 30 h and 40 h. The EBM fabricated samples were cooled slowly to 100 °C in 10 h and were then taken out of the vacuum chamber and cooled to room temperature in air. Finally, these EBM samples were cut from the bottom plate by wire-electrical discharge machining.

[1] This selected build temperature was high enough to ensure powder sintering. A higher build temperature would lead to a fact that EBM-built parts cannot be removed from the surrounding powders. The measured starting plate temperature was above 1020 ºC for the whole process.

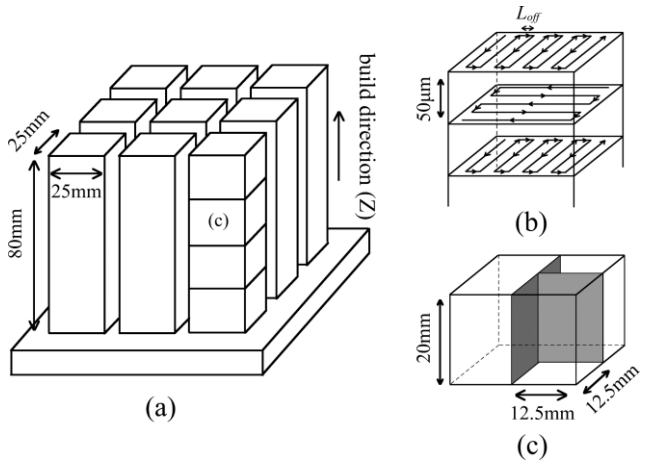

Fig. 1. Schematic diagrams of (a) one batch of as-EBM DZ125 samples; (b) electron beam scans in a snake-like way with a specific L_{off} and the hatching direction is changed by 90° after each build layer of 50 μm; (c) the EBM sample position where metallographic specimens were extracted for microstructural evaluations. Note: the indicated (c) in Fig. 1(a) represents the microstructural characterisation region as shown in Fig. 1(c).

Table 2 shows the chemical composition of plasma rotating electrode process (PREP) DZ125 powders. This composition is the same to cast DZ125. Fig. 2(a) shows the round-shaped morphology of the DZ125 powders, while Fig. 2(b) shows the microdendritic structure of a single ground and polished powder. Particle size distribution, Fig. 2(c), obtained by laser diffraction analysis, shows that 80 vol.% of DZ125 powders are within the size range between and 54 μm and 119 μm.

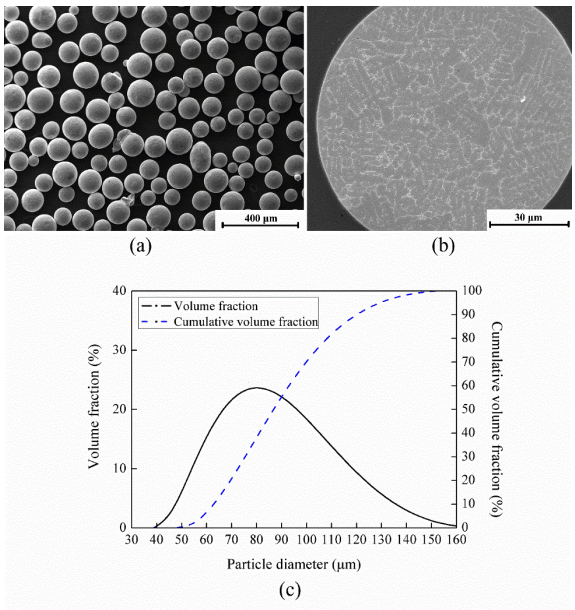

Fig. 2. SEM micrographs and particle size distribution of pre-alloyed DZ125 powders: (a) the powder morphology, (b) a single ground and polished powder particle showing microdendritic structure, and (c) volume fraction distribution and cumulative volume fraction of powder particles.

2.2. Post-processing heat treatment

Sample 3 with a coarse columnar grain structure and sample 4 with a fine columnar grain structure (abbreviated as CCG and FCG in Table 1) in as-EBM condition were subjected to post-processing that consisted of HIP and STA. These two samples (one representing CCG and the other representing FCG) were selected as it was reported in [25] that crack formation was related to columnar grain width in an EBM-built γ' precipitation-strengthened nickel-base superalloy. HIP was mainly carried out at 1230 °C (γ'-solvus[2]) and 150 MPa for 4 h, followed by furnace cooling to room temperature. This HIP condition is henceforth referred to as EBM+HIP. Selected EBM+HIP samples 3 and 4 were then subjected to STA. The STA heat treatment included first solution treating at 1180 °C for 2 h and then at 1230 °C for 3 h, followed by rapid cooling to room temperature; second γ' precipitation ageing at 1100 °C for 4 h and then ageing at 870 °C for 20 h, followed by rapid cooling to room temperature. This condition is referred to as EBM+HIP+STA. The STA condition was selected according to the standard heat treatment procedure for the cast material [26], although a shorter time of solution heat treatment could be used for the EBM-built [27]. The γ' ageing temperature used for DZ125 is close to that of 1121 °C used for Rene 142 [28]. HIP condition at 1280 °C and 150 MPa for 4 h was also performed on as-EBM condition to help clarifying cracking mechanism, because it was suggested by Roncery et al. [1] that HIP temperatures above γ'-solvus resulted in a greater efficiency of the porosity reduction. This HIP condition is referred to as 1280 °C HIP and the subsequent STA condition is referred to as 1280 °C HIP+STA.

2.3. Metallography

Optical microscopy (Leica DM 4000) was used to examine γ grain structure. Specimens were cut parallel to the build direction (Z-direction), from the centre position of the EBM-built samples (i.e. away from the contour melting areas). They were ground with 60 to 2000 grit SiC papers, then polished with 1 μm diamond suspension and finally etched in a Kalling's solution. Grain length and width measurements were performed using the mean linear intercept method, according to

[2] Differential scanning calorimetry was employed to determine the γ'-solvus temperature.

[29]. The grain aspect ratio was then derived for each specimen.

A JEOL JSM7100F field emission gun scanning electron microscopy (FEG-SEM) equipped with an electron backscattered diffraction (EBSD) detector was used to map grain orientations. EBSD maps were obtained with a 5 μm step size over large areas, and data were analysed by OIM software. Specimens were cut perpendicular to the build direction, i.e. X-Y plane was examined. They were ground with 60 to 2000 grit SiC papers, polished with 1 μm diamond suspension and finally OPS polished with colloidal silica. In addition, the γ/γ' microstructure of samples 3 and 4 as well as cast DZ125 were characterised further by SEM (20 kV and mainly secondary electron SE mode) using a FEI Quanta 200F with an energy dispersive X-ray spectroscopy (EDS). To reveal γ' precipitates morphology, specimens were electro-etched using 5 V with a solution of 70 ml H_3PO_4 and 30 ml H_2O for 4 seconds. A minimum of 100 γ' precipitates were analysed to quantify γ' size (edge length), γ' volume fraction as well as γ channel width.

Samples 3 and 4 in both EBM and EBM+HIP+STA conditions were used to study the cracking mechanism. Optical microscopy and SEM were applied to observe the crack morphology on X-Z plane. The crack ratio method, as described in [30], was used to provide quantitative analysis on the number density of cracks. In brief, the crack ratio was obtained from evaluation of both the length and width of each crack and then the total cracked area was divided by the total area of each micrograph. A minimum of 100 cracks were analysed from a total of 10 micrographs. In addition, cracked surfaces were examined by SEM. This method was judged in [30, 31] as the best approach to distinguish the liquid-state cracking from solid-state cracking mechanism for nickel-base superalloys.

Unless otherwise specified, all metallography examinations were performed at the same height of Z=50 mm, i.e. 30 mm below the top surface and near the centre of vertical and horizontal planes, as shown in Fig. 1(c). This allowed a comparative study of the influences of different EBM processing parameters on the microstructural evolution. The microstructural gradient in as-EBM sample 3 along the build direction (i.e. Z=10, 30, 50 and 70 mm) was also examined as Chauvet et al. [25] reported that a strong microstructural gradient along the build direction was found in an EBM-built non-weldable nickel-base superalloy ($23 \times 23 \times 30$ mm^3).

2.4. Mechanical testing

Micro-hardness (Hv200) measurements were performed on samples 3 and 4 in both as-EBM and post-processed conditions as well as the cast DZ125 samples. 20 measurement points per sample were performed at the same height of Z=50 mm and the average values are reported here. Micro-hardness measurements were also performed on as-EBM sample 3 along the build direction at Z=10, 30, 50 and 70 mm respectively to assess the influence of microstructural gradient.

M10 threaded-end round bar specimens with a 28 mm gauge length and 5 mm gauge diameter, were machined from samples 3 and 4 in EBM+HIP condition, with the load axis parallel to the build direction. Monotonic tensile tests at 850 °C with a constant cross-head displacement rate of 0.15 mm/s were performed on these specimens as well as the specimens made of cast+STA DZ125. These tensile tests were conducted in air on a Instron load frame equipped with a three-zone furnace and a 250 kN load cell.

3. Results

3.1. Grain structure

Both columnar and near-equiaxed grain structures can be obtained with different EBM parameters, Figs. 3(a)-(f). The average grain width and grain aspect ratio for each as-EBM sample are given in Table 1. The grain width increased with the decreasing v (or increasing E_A) from samples 1 to 3, Figs. 3(a)-(c) and Table 1. These three samples were fabricated with the same values of P and L_{off}, Table 1. Sample 4 (170.0±24.3 μm) had a coarser columnar grain structure compared to sample 5 (87.5±13.5 μm), Figs. 3(d) and (e), although these two samples were fabricated with the same value of E_A = 2.50 J/mm^2. This was achieved by increasing the proportion of v in the denominator of Eq. 1, while keeping the product of L_{off} and v as the same. Sample 6 was fabricated with the smallest value of L_{off} (the highest value of E_A=5.00 J/mm^2) compared to those samples exhibiting columnar grains. A near-equiaxed grain structure was obtained for sample 6. More precisely, this sample had a slightly elongated grain shape along the build direction, Fig. 3(f). EBSD IPF orientation

maps, Figs. 4(a)-(e), show that γ grains are orientated with their [001] parallel to the build direction for samples 1 to 5. The columnar grain structure with a strong [001] texture resulted from epitaxial growth starting with a face-centred-cubic phase and steep temperature gradients mostly parallel to the build direction. In contrast, the near-equiaxed grains for sample 6 had a relatively low preferred orientation, Fig. 4(f).

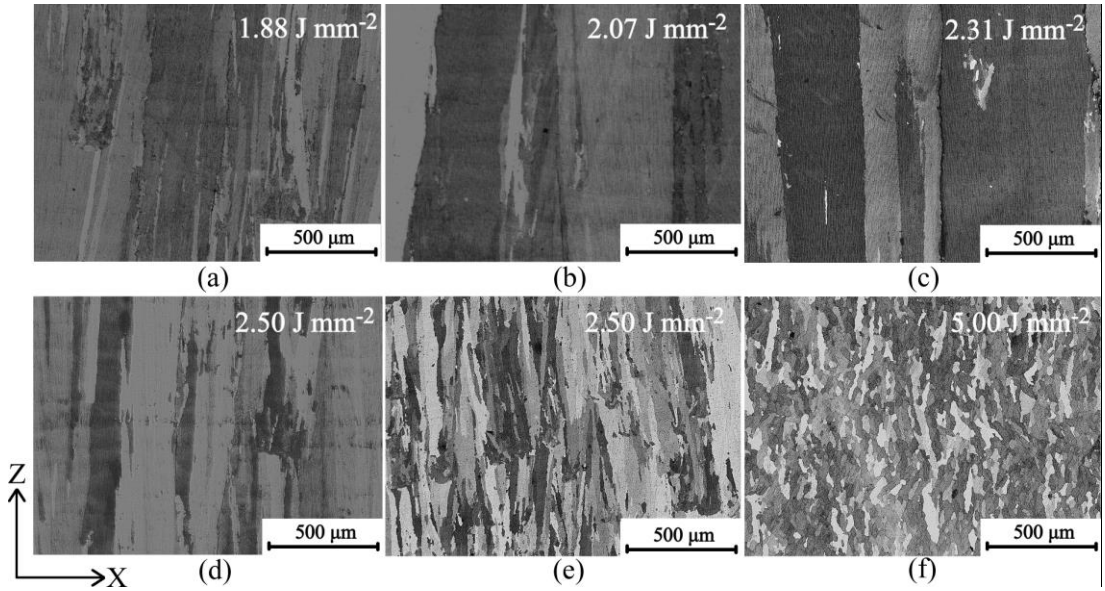

Fig. 3. Optical micrographs in the X-Z plane of DZ125 samples fabricated by EBM with different E_A values: (a) sample 1 with E_A=1.88 J/mm^2; (b) sample 2 with E_A=2.07 J/mm^2; (c) sample 3(CCG) with E_A=2.31 J/mm^2; (d) sample 4(FCG) with E_A=2.50 J/mm^2; (e) sample 5 with E_A=2.50 J/mm^2; (f) sample 6 with E_A=5.00 J/mm^2. Note: Numbers correspond to samples IDs given in Table 1.

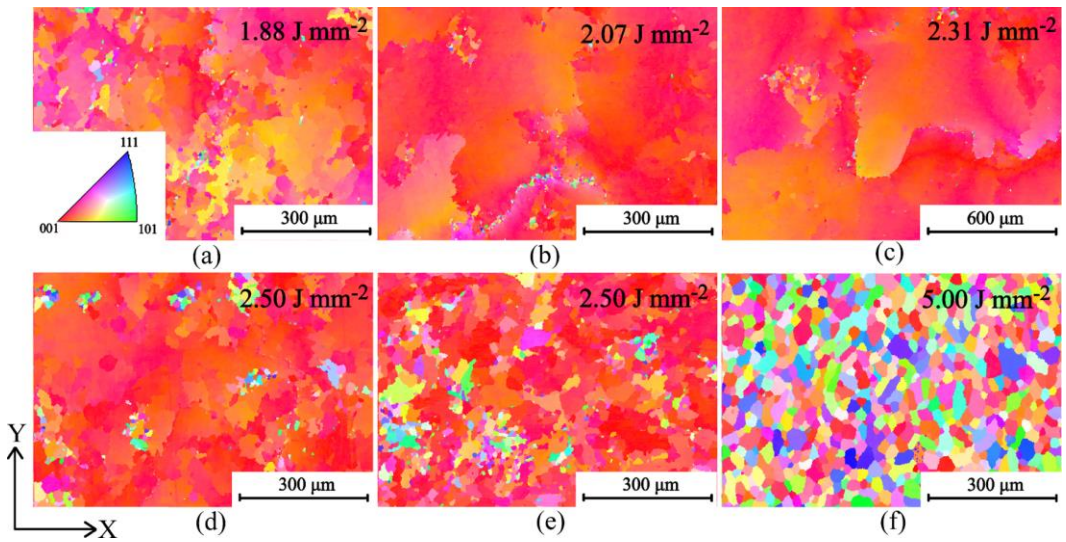

Fig. 4. EBSD γ-phase IPF orientation maps of DZ125 samples fabricated by EBM with different E_A values: (a) sample 1 with E_A=1.88 J/mm^2; (b) sample 2 with E_A=2.07 J/mm^2; (c) sample 3(CCG) with E_A=2.31 J/mm^2; (d) sample 4(FCG) with E_A=2.50 J/mm^2; (e) sample 5 with E_A=2.50 J/mm^2; (f) sample 6 with E_A=5.00 J/mm^2.

3.2. γ/γ' microstructure in as-EBM condition

Fig. 5(a) shows four columnar γ grains for as-EBM sample 3 (CCG). A fine dendritic structure (i.e. closely spaced dendrites) was observed within these columnar grains. Both the dendrite core and dendrite boundary are indicated in Fig. 5(b) for columnar grain C. Lines of MC carbide precipitates parallel to dendrite boundaries can be seen in Fig. 5(b). These MC carbides were also formed along columnar grain boundaries, as shown in Fig. 6(a). EDS analyses confirmed that they are Hf-rich, Table 3. A similar Hf-rich MC carbide was reported in EBM-built Rene 142 [13]. The schematic diagram in Fig. 6(b) delineates typical locations where these carbides are present. Fig. 7(a) shows the morphology of three parallel widely spaced dendrites in as-cast DZ125; secondary dendrites are also present. A typical dendrite width of as-cast condition was found to be between 300 to 400 μm, Fig. 7(a), that is two orders of magnitude larger than the dendrite width for the as-EBM sample, Fig. 5(b). Little difference in dendrite width (both within the size range of 300-400 μm) can be observed when the as-cast sample was subjected to the STA heat treatment, Fig. 7(b).

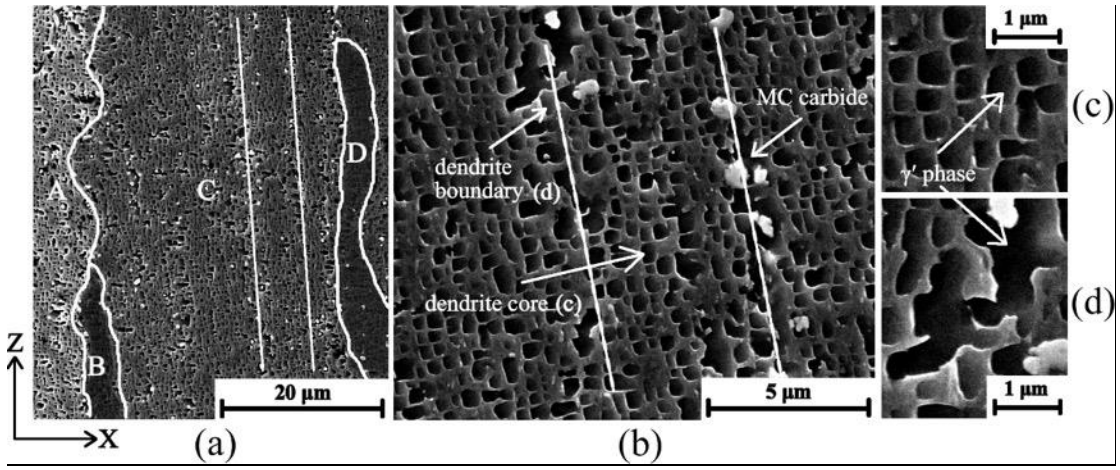

Fig. 5. SEM micrographs of as-EBM DZ125 sample 3(CCG) with a typical columnar grain structure: (a) low magnification SEM image showing different columnar grains as indicated from A to D; (b) high magnification SEM image showing dendrite core and dendrite boundary regions within the columnar grain C; (c) and (d) enlarged SEM images showing the presence of larger sized γ′ phase at dendrite boundary region.

In terms of γ' precipitation in as-EBM condition, smaller γ' were seen at dendrite cores, Fig. 5(c), when compared to those at dendrite boundaries, Fig. 5(d). This phenomenon can be also seen in Fig. 8(a) for sample 3 and in Fig. 8(b) for sample 4.

These heterogeneously distributed γ' (γ' clusters) in Figs. 8(a) and (b), most likely correspond to the dendrite boundaries as shown in Fig. 5(d). Figs. 8(c) and (d) show the γ' morphology for the as-cast and cast+STA condition, respectively. STA resulted in the presence of γ' with better defined facets (i.e. a cuboidal shape), Fig. 8(d), when compared to those with extended corners of the cuboids (a continued growth from the cuboidal shape) in as-cast condition, Fig. 8(c). The morphological development of γ' during ageing in a range of superalloys was studied in [32] and it was concluded that γ' developed in the sequence of spheres, cuboids with well defined facets, cuboids with extended corners along <111> direction, and arrays of cuboids. The γ' morphology in as-EBM condition tended to be more spherical shaped with less defined facets, Figs. 8(a) and (b), particularly when compared with that in cast+STA condition, Fig. 8(d). The measured γ' sizes for as-EBM samples 3 and 4 were similar, but they were smaller than those in as-cast condition, Fig. 9. In addition, γ' precipitates at the dendrite core of as-EBM samples were smaller than those at the dendrite boundary. An EBM post-processing heat treatment is required to promote homogeneously distributed, cuboidal shaped γ' precipitates with better defined facets as such a desired γ' morphology cannot be obtained in as-EBM condition, Figs. 8(a) and (b).

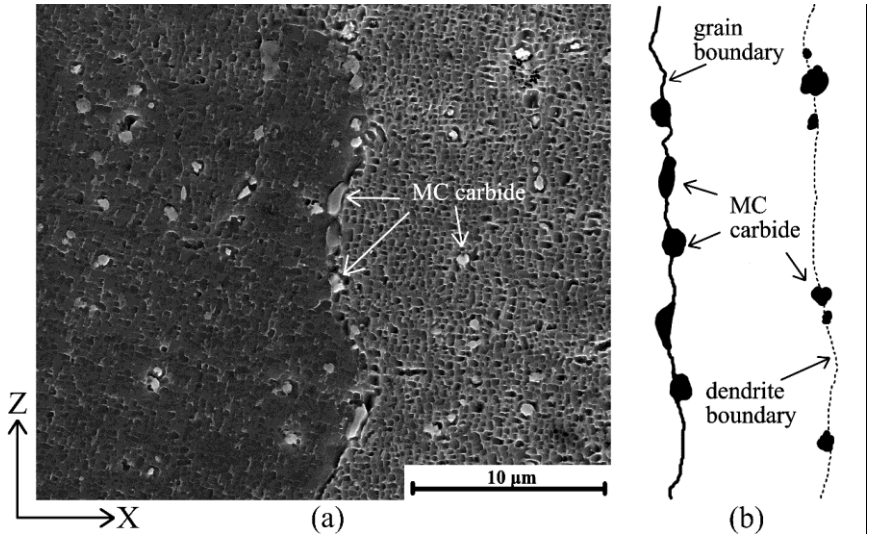

Fig. 6. (a) SEM micrograph in the X-Z plane of as-EBM sample 3(CCG) showing that MC carbides nucleate preferably at the columnar grain boundary and dendrite boundary regions; (b) a schematic diagram delineating the locations of MC carbides.

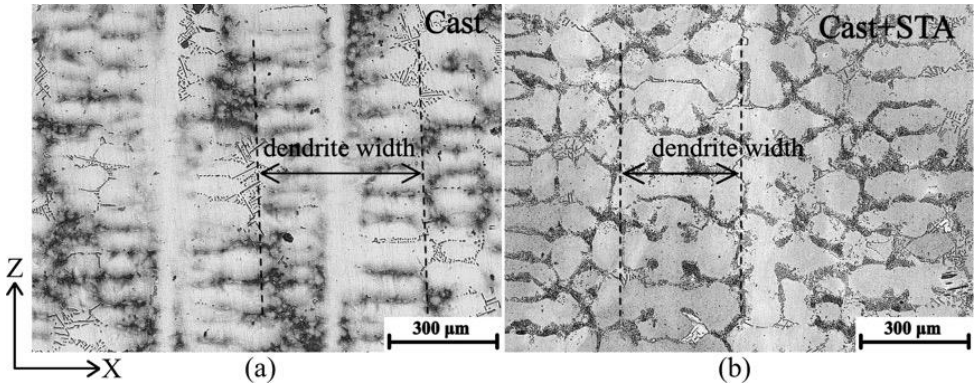

Fig. 7. Optical micrographs of cast DZ125: (a) as-cast and (b) cast+STA.

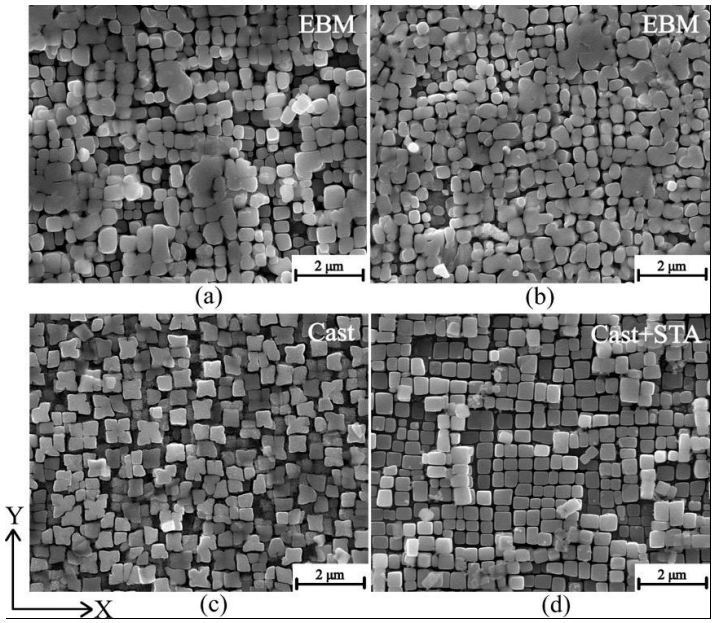

Fig. 8. SEM micrographs of as-EBM samples 3 and 4 as well as cast DZ125 samples showing the morphology of γ′ precipitates: (a) as-EBM sample 3 (CCG); (b) as-EBM sample 4 (FCG); (c) as-cast sample; (d) cast+STA sample.

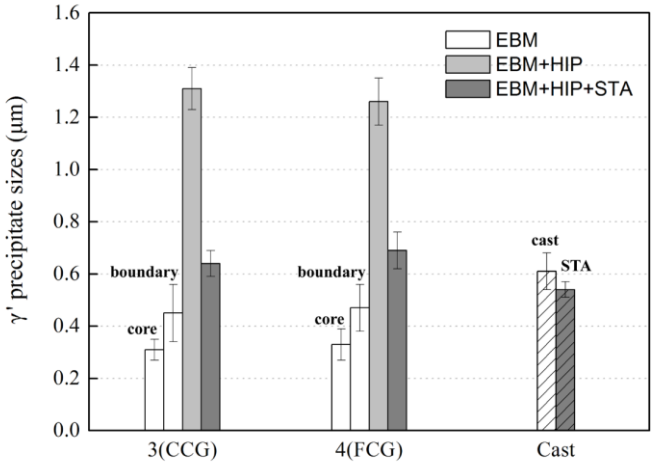

Fig. 9. Measured average size of γ′ precipitates of as-EBM samples 3 and 4 and their changes due to HIP and STA heat treatment. These are compared with the cast DZ125 in both as-cast and cast+STA conditions. The γ′ precipitates at dendrite core and dendrite boundary location are considered separately for the as-EBM condition.

3.3. Influence of post-processing on γ' morphology and size

As-EBM samples 3 and 4 were subjected to post-processing that consisted of HIP (1230 °C, 150 MPa, 4 h) and STA, as described in section 2.2. The presence of the so-called arrays of γ' cuboids with some extended corners can be clearly seen for samples 3 and 4 in EBM+HIP condition, Figs. 10(a) and (b). This was due to a relatively slow cooling rate (e.g. 150 °C/min) provided by the most commonly-used HIP facility. When the HIPped samples were subjected to subsequent STA heat treatment, the presence of γ' precipitates with better defined facets (i.e. a cuboidal shape) can be seen in Figs. 10(c) and (d) for samples 3 and 4, respectively. Such a γ' morphology is similar to that obtained in cast+STA DZ125, Fig. 8(d).

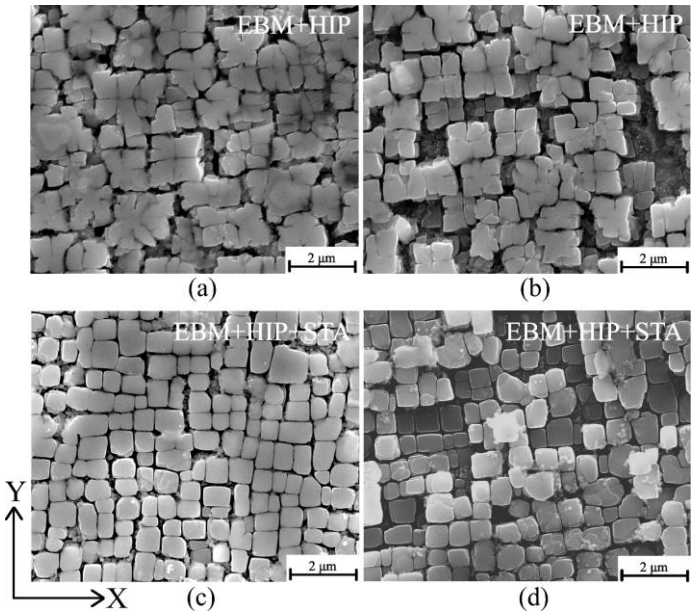

Fig. 10. SEM micrographs of γ′ phase in the X-Z plane of EBM-built DZ125 alloys: (a) and (b) EBM+HIP condition for samples 3 (CCG) and 4 (FCG); (c) and (d) EBM+HIP+STA condition for samples 3 (CCG) and 4 (FCG).

In terms of γ' size, HIP led to a significant increase in their size, whereas HIP+STA resulted in a reduction in their size, Fig. 9. There was little size difference in γ' precipitates between the dendrite core and dendrite boundary areas for the EBM+HIP and EBM+HIP+STA conditions, thus the reported γ' size in Fig. 9 reflects the average of the dendrite core and boundary for the post-processed conditions. When compared to the cast+STA condition, samples 3 and 4 in EBM+HIP+STA condition had slightly larger γ' sizes, Fig. 9. The γ' size, γ' volume fraction and γ channel width are

summarised in Table 4. Measurement errors in Table 4 and Fig. 9 reflect the standard deviation from the average value. Compared to the as-EBM condition, HIP led to both an increased γ channel width and γ' size but little change in γ' volume fraction. HIP+STA resulted in both a decreased γ channel width and γ' size but an increased γ' volume fraction. In addition, there was little difference between samples 3 (CCG) and 4 (FCG) in terms of γ' features, Table 4.

3.4. Cracking behaviour

The presence of cracks primarily parallel to the build direction were found for both samples 3 (CCG) and 4 (FCG) in as-EBM condition, Figs. 11(a) and (b). These EBM induced cracks are exclusively formed at columnar grain boundaries that were decorated with MC carbides, Figs. 11(c) and (d). Although lines of MC carbides were also formed along dendrite boundaries, no cracks were found at these locations, Figs. 11(c) and (d). This indicates that the occurrence of EBM induced cracks should not be solely attributed to MC carbides. As already reported in several studies [21, 25, 31, 33], cracking in nickel-base superalloys could depend on the degree of grain boundary misorientation, level of grain boundary micro-segregation, and other factors.

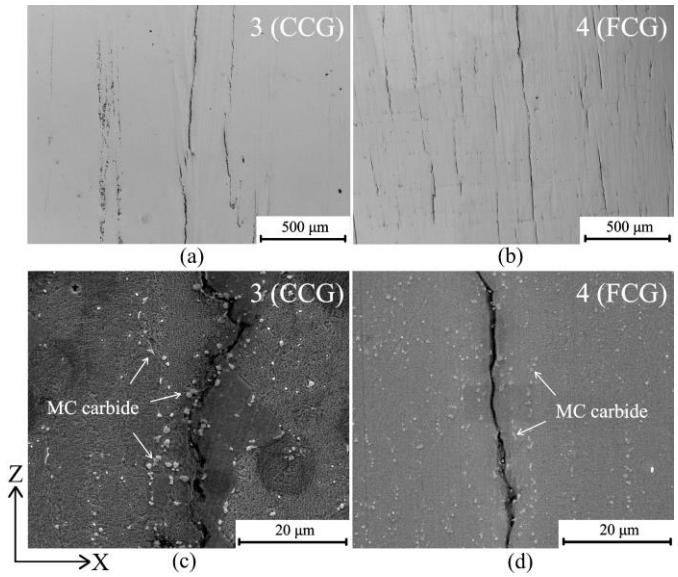

Fig. 11. Crack morphology of as-EBM DZ125: (a) and (b) optical micrographs of samples 3 (CCG) and 4 (FCG) showing the cracks along the columnar grain boundaries; (c) and (d) SEM micrograph of samples 3 and 4 showing the distribution of MC carbides close to the cracked grain boundary region and dendrite boundaries.

HIP at 1230 °C and at 150 MPa for 4 h were applied to close these intergranular cracks. It is worthwhile to note that all free surfaces of cracked EBM samples were initially sealed by electron beam re-melting; this thereby removes any possible surface cracks. In other words, no surface cracks that are open to the surface of EBM samples and hence could prevent the healing effect of the HIP. Figs. 12(a) and (b) show that these EBM induced intergranular cracks were healed to some extent but residual pores existed in HIP condition. However, the reappearance of intergranular cracks was observed for the subsequent STA condition, Figs. 12(c) and (d). There are two important features regarding these cracks. First, the crack opening width for the EBM+HIP+STA condition, Figs. 12(c) and (d), was much larger than that for as-EBM condition, Figs. 11(c) and (d). This phenomenon suggests that there was a higher tensile stress perpendicular to the crack face to pull the cracks apart as a result of the STA treatment. Second, much higher crack ratios were found for samples in EBM+HIP+STA condition, Figs. 12(c) and (d) compared to those in as-EBM condition, Figs. 11(a) and (b). For a quantitative comparison, measured crack ratios for each sample condition are summarised in Table 4. A significant decrease in crack ratios for the EBM+HIP condition can be seen in Table 4, when compared to the as-EBM condition. For example, sample 3 in EBM condition had a crack ratio of 2.60%, and this value reduced to 1.29% in EBM+HIP condition, Table 4. When sample 3 was subjected to a further STA treatment, a much higher crack ratio of 5.69% was observed in EBM+HIP+STA condition, Table 4. Sample 4 exhibited a similar trend in terms of the crack ratio change, Table 4. The small crack ratio values for samples 3 and 4 in EBM+HIP condition correspond to the number density of pores as illustrated in Figs. 12(a) and (b).

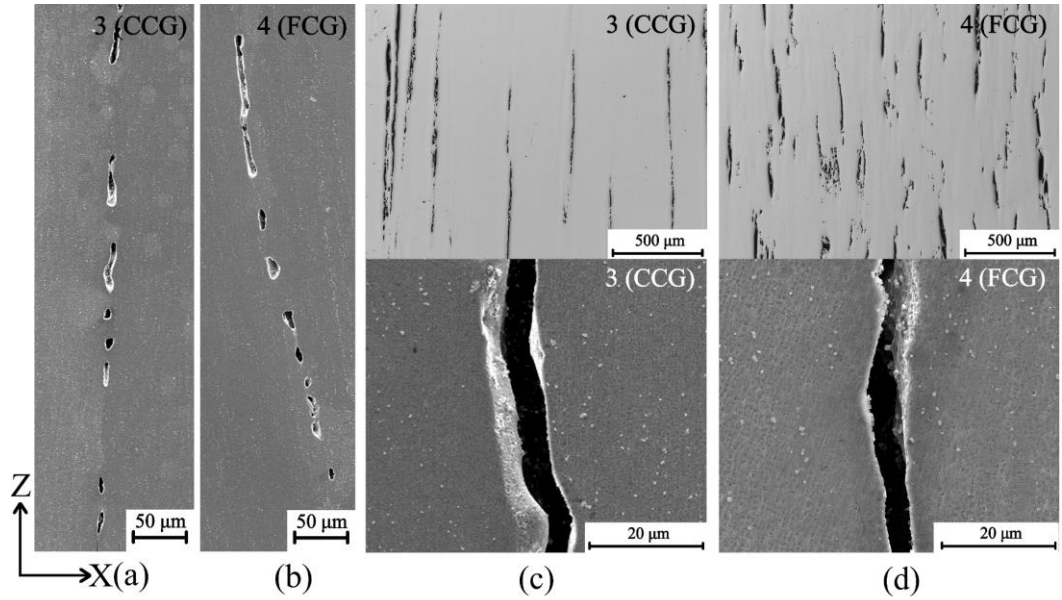

Fig. 12. SEM and optical micrographs showing reappearance of intergranular cracks due to the post-processing: (a) and (b) samples 3 and 4 in HIP condition; (c) and (d) samples 3 and 4 in HIP+STA condition. Upper two figures in (c) and (d) are optical micrographs of polished specimens and the lower two figures are SEM micrographs of etched specimens.

Additional experiments (HIP at 1280 °C and 150 MPa for 4 h) were performed on selected EBM+HIP+STA samples 3 and 4, as described in section 2.2. These HIP experiments aimed to confirm that reappearance of intergranular cracks in EBM+HIP+STA condition should not be primarily attributed to the presence of residual pores in samples that had been initially HIPped at 1230 °C. Fig 13 shows the crack evolution and γ' precipitation in sample 4 as a result of 1280 °C HIP and STA treatment. A similar phenomenon was observed for sample 3 and thus micrographs are not shown here. 1280 °C HIP resulted in an almost crack-free microstructure, Fig. 13(a). The crack ratio in 1280 °C HIP sample 4 was measured to be 0.28%, that is much lower than that obtained in HIP at 1230 °C (i.e. 1.03% for sample 4 in EBM+HIP condition, Table 4). However, intergranular cracks reappeared when 1280 °C HIP sample 4 was subjected to a further STA treatment, Fig. 13(b). The crack ratio for sample 4 in 1280 °C HIP+STA condition was measured to be 4.83%, that is very similar to that found in EBM+HIP+STA condition having a crack ratio of 4.93%, Table 4. Again, these post-processing induced cracks, Fig. 13(b), had a much higher crack opening width than the EBM induced cracks, Fig. 11(b). As expected, HIP at 1280 °C led to γ' cuboids with some extended corners, Fig. 13(c), but a further STA

treatment restored γ' cuboids with well defined facets, Fig. 13(d).

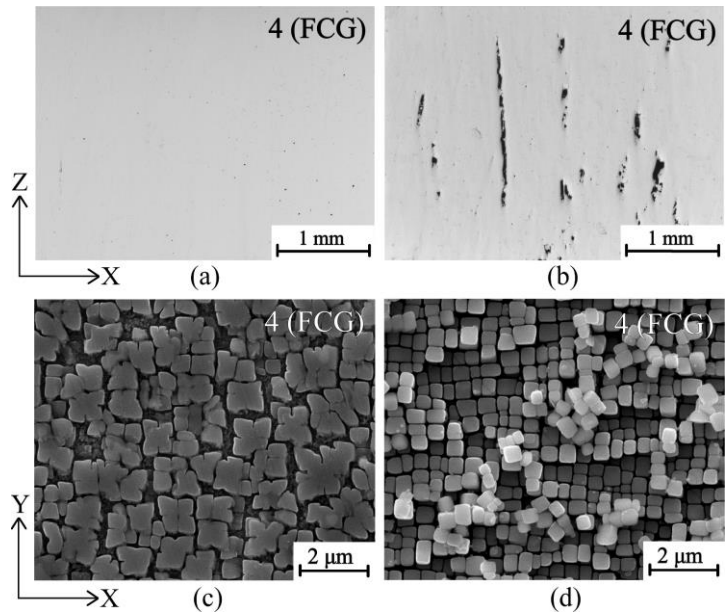

Fig. 13. Optical and SEM micrographs of sample 4: (a) 1280°C HIP condition showing that EBM induced cracks can be fully closely with an increasing HIP temperature; (b) 1280°C HIP+STA condition showing the reappearance of intergranular cracks; (c) and (d) γ′ precipitates morphological evolution as a result of 1280°C HIP and STA treatment.

3.5. Mechanical properties

The micro-hardness of sample 3 (CCG) decreased from ~475 Hv in the as-EBM condition to ~450 Hv in both the HIP and HIP+STA conditions, Fig. 14(a). A similar reduction in micro-hardness was found for sample 4 (FCG), Fig. 14(a). In contrast, the cast DZ125 had a micro-hardness increase of ~50 Hv resulting from the STA treatment, Fig. 14(a). The lower micro-hardness in EBM+HIP+STA condition compared to that in cast+STA condition could be due to a slightly larger γ' precipitate size in the former.

High temperature (850 °C) tensile test results of samples 3 and 4 in EBM+HIP condition are shown in Fig. 14(b). In general, both the yield strength and ultimate tensile strength of the EBM-built samples in EBM+HIP condition are comparable to those in cast+STA condition. The slightly lower tensile strength in EBM+HIP samples can be related to the presence of γ' cuboids with some extended corners, Figs. 10(a) and (b). Since significant numbers of cracks were already observed in both

samples 3 and 4 in EBM+HIP+STA condition, Table 4, no high temperature tests were performed on those samples. Similarly, no high temperature tensile test was performed on as-EBM samples because of the observed intergranular cracks.

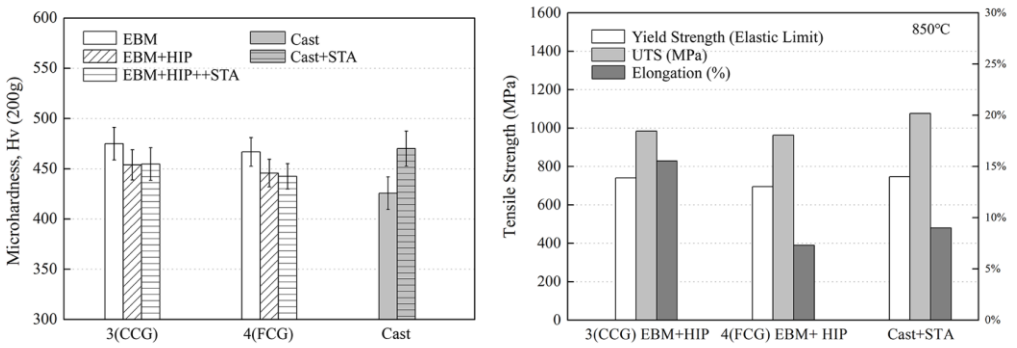

Fig. 14. (a) Room temperature Vickers hardness measurements on EBM-built samples 3 and 4 as well as cast DZ125; (b) Monotonic tensile tests at 850 °C on samples 3 and 4 in HIP condition as well as cast DZ125 sample in STA condition.

4. Discussion

4.1. Relationship between EBM processing and grain structure

In the as-EBM condition, columnar grains that grow epitaxially along the build direction were found in samples 1 to 5, Figs. 3(a) to (e). Near-equiaxed grain structure with a grain aspect ratio of 3.4±0.5 were found in sample 6, Fig. 3(f) and Table 1, that had been fabricated with the smallest L_{off} (i.e. a higher overlap of melting tracks). Numerical simulations of the EBM melting process were applied in [7] to study underlying mechanisms responsible for the presence of columnar and equiaxed grain structures in Inconel 718. It was concluded that (i) a smaller v tended to create a columnar grain structure and (ii) a smaller L_{off} (i.e. a higher overlap of melting tracks led to a more equiaxed grain structure. Smaller v increases the energy density in the local melt pool such that it decreases thermal gradient and hence promotes the formation of equiaxed grains. This could also explain the effect of L_{off}. The observed changes in columnar grain width from samples 1 to 3 with decreasing v and from samples 4 to 6 with decreasing L_{off}, Table 1, are therefore consistent with previous work [7].

Careful examinations of the columnar grain width at different Z height positions

(i.e. Z=10, 30, 50 and 70 mm) along the build direction was performed on as-EBM sample 3. The columnar grain width increased from 542.6±17.2 μm at Z=10 mm to 886.5±19.3 μm at Z=70 mm, Table 5. An increasing columnar grain width along the build direction (a total build height of 30 mm) was also reported in an EBM nickel-base superalloy [25], where the grain width was found to increase significantly from ~150 μm at Z=10 mm to ~800 μm at Z=25 mm. This very large gradient in grain width was attributed to the hot zone (top surface layers under EBM fabrication) and cold zone (underlying layers that was less affected by the building process), analogous to single crystal growth by the Bridgman method [25]. It must be pointed out that a relatively homogeneous grain structure would be expected for the conventional Bridgman crystal-growing method, provided that the withdrawn rate and solidification condition was not changed in purpose during the whole process.

During EBM fabrication, each new layers are pre-heated to the pre-defined build temperature by defocused electron beam prior to the melting process. This ensures that the initial boundary conditions for solidification of the subsequent deposited layers is independent of build height in theory. In other words, the heat input provided by electron beam to create the melt pool should be very similar for each new layers with a square geometry of 25 × 25 mm^2, Fig. 1(a). However, the heat can be conducted evenly through all three directions (x, y and z) when the build is closer to the substrate powder bed. As the build height increases, the heat transfer along the build direction becomes more dominant and this indicates that solidification condition varies with build height. It was postulated by Tan et al. [34] that the cooling rate (the heat transfer by thermal conduction) decreased with the increasing build height of EBM Ti-6Al-4V. They further attributed the presence of a moderate increase in prior β grain width from 42.77±14.52 μm at the bottom to 56.82±13.73 μm at the top (a total build height of 40 mm) to the cooling rate difference. Therefore, the presence of a moderate increase in columnar grain width along the EBM build direction for the present nickel-base superalloy (a total build height of 80 mm) could be justified. In addition, there was less grain width change in the first 30 mm build height (542.6±17.2 μm at Z=10 mm, 593.8±20.7 μm at Z=30 mm) compared to the last 30 mm build height (700±18.9 μm at Z=50 mm, to 886.5±19.3 μm at Z=70 mm). This indicates that the cooling rate changed non-linearly with the increase in build height.

4.2. Relationship between EBM processing and γ' precipitation

Samples 3 (CCG) and 4 (FCG) in as-EBM condition, dendrite core regions, have γ' sizes of 0.31±0.04 μm and 0.33±0.06 μm, and γ' volume fractions of 64% and 70%, respectively, Table 4. Both the γ' size and volume fraction in as-EBM DZ125 are similar to those found in as-EBM CMSX-4 (0.35 μm and 72%) [23] and Rene 142 (0.28 μm and 59%) [13]. A detailed study on the γ' morphology in as-EBM DZ125 revealed that dendrite boundaries had larger and heterogeneously distributed γ' precipitate clusters, Figs. 8(a) and (b). The work by Ruttert et al. [24] also revealed that a roughly twice as large for the γ' precipitates in as-EBM CMSX-4 were at dendrite boundaries compared to dendrite cores. In addition, spherical shaped and facets less defined γ' are present in as-EBM condition, Figs. 8(a) and (b). It is well-known that both the size and morphology of γ' precipitates are important in determining the γ/γ' lattice misfit (i.e. the pinning effects of γ' precipitates on dislocations) [15, 35], and hence a cuboidal shape offers the best high temperature mechanical properties of superalloys [32]. Therefore, a homogenisation heat treatment is needed for the EBM-built γ' precipitation-strengthened superalloys to dissolve primary γ' precipitates and then to promote a more uniformly distributed and more cuboidal shaped γ' by ageing treatment.

Previous studies [23, 25] reported that the presence of gradient in γ' size from the bottom to the top of the build can be attributed to the EBM process-inherent *in situ* heat treatment (i.e. long-time exposure to the high build temperature). An EBM build temperature of 950 ºC was used to fabricate CMSX-4 (a total height of 25 mm) in [23]. As a consequence, the γ' coarsening phenomenon was found at the bottom of the build (~0.4 μm at Z=10 mm), when compared to the the regions near to the top surface (~0.2 μm at Z=24 mm) [23]. It is important to note that 950 ºC is within the typical γ' precipitate ageing temperature for CMSX-4. This indicates that the undesirable γ' size gradient in as-EBM condition could be avoided by using an EBM build temperature that is lower than the precipitate ageing temperature. To prove this hypothesis, the EBM build temperature of 1050 °C was selected for the present DZ125 (the first/primary step γ' ageing is 1100 °C). As shown in Table 5, the γ' size

in as-EBM condition changed from 0.40±0.06 μm at Z=10 mm to 0.35±0.05 μm at Z=70 mm at the dendrite core, indicating that the *in situ* heat treatment effects can be minimised by using a more appropriate EBM build temperature. In other words, the EBM build temperature that is lower than primary γ' ageing temperature facilitates the creation of build height independent γ' precipitates. A lower micro-hardness was obtained for the sample position at Z=10 mm compared with that at Z=30, 50 and 70 mm, Table 5. This corresponds to the slightly larger γ' precipitates and lower γ' volume fraction in the former.

4.3. Cracking mechanism

The intergranular cracks were found to align along the build direction and exclusively at columnar grain boundaries, as shown in Fig. 11 for as-EBM condition, Figs. 12 (c) and (d) for EBM+HIP+STA condition, and Fig. 13(b) for 1280 °C HIP+STA condition. The difference between the EBM and post-processing induced cracking is that the latter had higher crack opening width and crack ratio. This suggests that the underlying mechanisms for crack formation could be different and thus deserves a detailed discussion. It is worth to mention that the present work represents the first study to report the occurrence of EBM post-processing induced cracks, although the presence of EBM induced cracks have been reported for example in [13, 24, 25].

4.3.1. EBM induced cracks

When plotting the 5.05 wt% Al and 1.04 wt% Ti contents (both are γ′ forming elements) in the classic superalloys weldability diagram, that was originally proposed by Prager and Shira and later modified by DuPont et al. [15], DZ125 is considered non-weldable due to its high susceptibility to cracking during welding or post-weld heat treatment. Based on the welding literature [15, 30, 33, 36-39], four potential cracking mechanisms could be responsible for the EBM induced crack formation: (i) liquation cracking; (ii) solidification cracking, also called hot tearing; (iii) ductility-dip cracking and (iv) strain-age cracking. Liquation cracking and solidification cracking are mechanisms that require the presence of liquid films whereas ductility-

dip cracking and strain-age cracking are mechanisms that occur at the solid state.

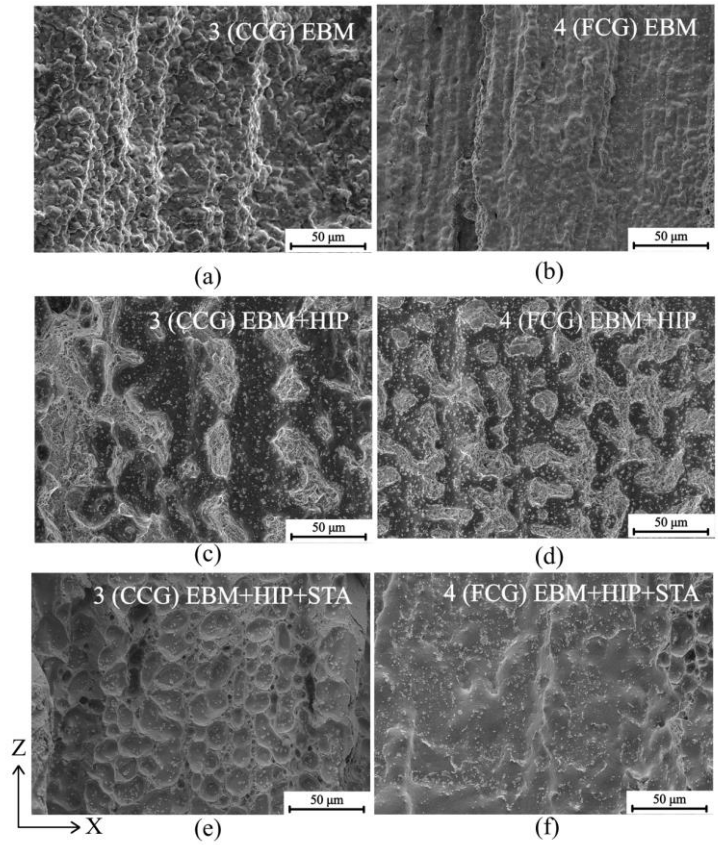

Fig. 15. SEM fractography examination of the cracked surfaces: (a) as-EBM sample 3; (b) as-EBM sample 4; (c) EBM+HIP sample 3; (d) EBM+HIP sample 4; (e) EBM+HIP+STA sample 3 and (f) EBM+HIP+STA sample 4

The SEM observation of the cracked surfaces of as-EBM samples 3 (CCG) and 4 (FCG), Figs. 15 (a) and (b), show the line-by-line structure of dendritic morphology. The presence of round shaped objects on the cracked surfaces corresponds to dendrite arm surfaces. These cracked surface characteristics lead to the judgement that there were liquid films remaining at columnar grain boundaries when the intergranular cracks formed in as-EBM samples. Therefore, EBM induced cracks in DZ125 can be classified as solidification cracking or liquation cracking. According to [40], solidification cracking occurs in the fusion zone during the solidification of the weld metal, whereas liquation cracking occurs in the partially melted zone. It is difficult to differentiate one from another for EBM, because the EBM melting process is known to include melting, re-melting and etc. In other words, it is impossible to track the crack location back to the fusion zone and hence solidification cracking mechanism, or partially melted zone and hence liquation cracking mechanism. Due to these complexities, the liquid-state cracking mechanism was not further investigated, but is

acknowledged to be solidification, liquation cracking, or some combination of the two mechanisms. The terminology of liquid-state cracking is hence used in the present work to reflect observed experimental evidence in Figs. 15 (a) and (b) that crack formation requires the presence of liquid films.

The mechanism responsible for the presence of EBM induced cracks in γ' precipitation-strengthened nickel-base superalloys (CMSX-4 in [24] and an unspecified type in [25] as well as the DZ125 in the present work) can be attributed to the presence of liquid films along grain boundaries and hence liquid-state cracking. This cracking mechanism is also responsible for crack formation in Inconel 738LC fabricated by SLM [21]. The formation of EBM induced cracks by the liquid-state cracking mechanism would require the development of tensile residual stresses caused by solidification shrinkage and thermal contraction of the solid. While the electron beam scans (hatch melting), the rear of the local weld pool is solidifying and contracting during cooling, thus creating tensile stresses in this region as the previously solidified layers act as a constraint. If the magnitude of tensile stresses exceeds the grain boundary cohesive strength in the presence of liquid films, cracking can occur. However, it should be mentioned that the magnitude of residual stresses is generally much lower in EBM process compared to the SLM additive manufacturing process, because the EBM powder bed is pre-heated to a high temperature (e.g. 1050 °C in the present work), that helps reducing the temperature gradients during local melting and solidification of the molten material.

Franklin and Savage [41] studied the cracking susceptibility in Rene 41 weldment, a γ' precipitation-strengthened nickel-base superalloy, by performing creep stress relaxation experiments on both solution annealed and γ'-overaged material conditions. It was found that in the solution annealed material the stress reduced at first due to creep under a fixed displacement, but after a short period of time began to increase and reach a stress peak after which the stress decreased. In comparison with the solution annealed material, the γ'-overaged material exhibited stress reduction continuously and there was no stress increase over the whole creep stress relaxation test. The creep stress relaxation interruption by a period of increasing stress in solution annealed material, was attributed to the ageing contraction accompanying γ' precipitation [41]. This interesting work indicates that the γ' precipitation process could also result in the creation of tensile stresses at the two surfaces of liquid films

and hence tend to pull apart the columnar grain boundaries. Therefore, it is very likely that the combined action of global constraint stresses and γ' precipitation induced stresses led to the crack formation in EBM-built DZ125 and other similar γ' precipitation-strengthened superalloys. Unfortunately, a precise estimate of γ' precipitation induced stresses during the EBM process cannot be done, owing to the complex thermal path. However, an indirect evidence to support this γ'-ageing contraction theory will be given in section 4.3.2 when discussing post-processing induced cracks.

Ramsperger et al. [23] performed a set of EBM parametric study to explore the crack mitigation strategy in CMSX-4. It was found that the combination of high beam powers, low scanning speeds and high build temperatures of >950 °C could result in crack-free microstructures of EBM-built CMSX-4. As already described in section 4.2, the high build temperature (i.e. close to or above γ' precipitate ageing temperature) selected for EBM CMSX-4 resulted in γ' size gradient from the bottom to the top of the build. To this end, HIP process was employed in the present work to close EBM induced internal cracks.

4.3.2. EBM post-processing induced cracks

HIPping (1230 °C, 150 MPa, 4 h) resulted in a significant crack ratio reduction from 2.72% in as-EBM condition to 1.03% in EBM+HIP condition for sample 4, Table 4. An increased HIP temperature of above γ'-solvus (1280 °C, 150 MPa, 4 h) created an almost crack-free microstructure, as illustrated in Fig. 13(a). This finding is consistent with the HIP work performed by Roncery et al. [1], where a greater efficiency of the porosity reduction was obtained by using HIP temperatures of above γ'-solvus. Although the successful crack closure can be achieved by HIPping, the reappearance of intergranular cracks associated with the STA heat treatment challenges the success of HIP in closing liquid-state cracks. Similar to the approach used to reveal the liquid-state cracking mechanism for EBM induced cracks, the cracked samples 3 and 4 in both the EBM+HIP and EBM+HIP+STA condition were fractured to open up the cracked surfaces. The SEM observation of cracked surfaces of EBM+HIP samples 3 (CCG) and 4 (FCG), Figs. 15 (c) and (d), show the presence of both relatively flat surfaces (darker areas of SEM image) and ductile fracture

surfaces (lighter areas of SEM image). These flat surfaces were probably created by the hydrostatic pressure applied in the HIP process. Hence it is likely that the liquid films induced by the original EBM process were not fully healed for both samples 3 and 4 in EBM+HIP condition. Finally, Figs. 15 (e) and (f) show the presence of round shaped objects and relatively flat surfaces in cracked surfaces of EBM+HIP+STA samples 3 (CCG) and 4 (FCG). To ascertain this experimental observation, additional samples 3 and 4 in EBM+HIP+STA condition were fractured for crack surface examination. All cracked surfaces exhibited the residual liquid film feature, similar to those shown in Figs. 15 (e) and (f). Therefore, this leads us to conclude that HIP cannot heal EBM induced liquid-state cracks. Since the cracking mechanism for the EBM post-processing is clarified, a better understanding of the presence of the larger crack opening width, Figs. 12(c) and (d), and the higher crack ratio, Table 4, for these post-processed samples needs to be developed.

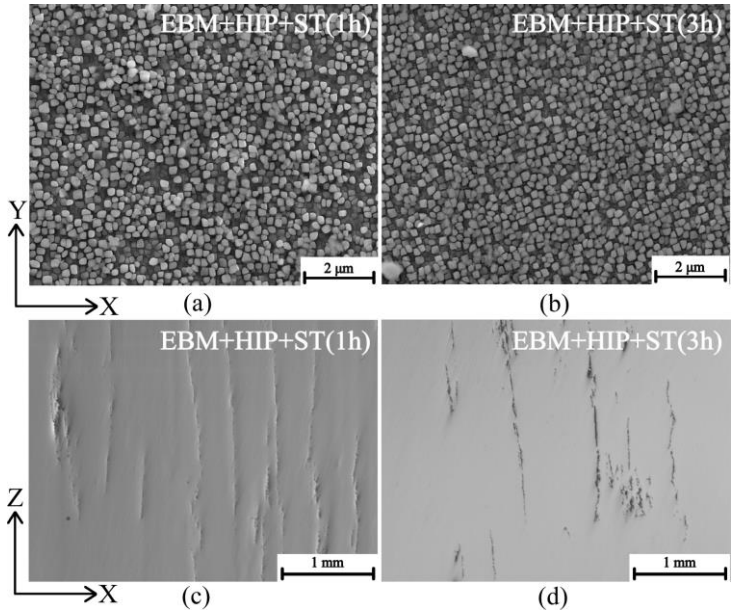

Fig. 16. SEM micrographs of γ′ precipitates evolution and cracking in sample 3 with the initial condition of EBM+HIP: (a) heat to 1230 °C and hold for 1 h, finally cooled to room temperature; (b) heat to 1230 °C and hold for 3 h, finally cooled to room temperature; (c) and (d) observed intergranular cracks for each condition by optical microscopy.

A design-of-experiment including three identical specimens for crack investigation was performed on sample 3 (CCG) in EBM+HIP condition to find out at what stage of the solution treating and ageing (STA) cycle these cracks formed. The first specimen was subjected to an ageing treatment without prior solution treating (ST), i.e. heat to

γ' ageing at 1100 °C for 4 h and then ageing at 870 °C for 20 h, followed by rapid cooling to room temperature. No cracking was observed in this specimen, thus this narrowed down the focus of our investigation to the solution treating step. The second and third specimens were heated to 1230 °C and held for 1 h and 3 h respectively to study the possible effect of solution treating on the crack formation. It is interesting to note that reappearance of intergranular cracks occurred for both specimens, Figs. 16(c) and (d), indicating that these cracks were associated with the ST step. Figs. 16(a) and (b) show SEM micrographs of γ′ precipitates in these two specimens. Both specimens exhibited very fine γ′ precipitates; they were formed during the cooling stage to room temperature. This indicates that the overaged γ' in EBM+HIP sample, Figs. 10(a) and (b), must have experienced γ' dissolution and then re-precipitation during the whole solution treating process.

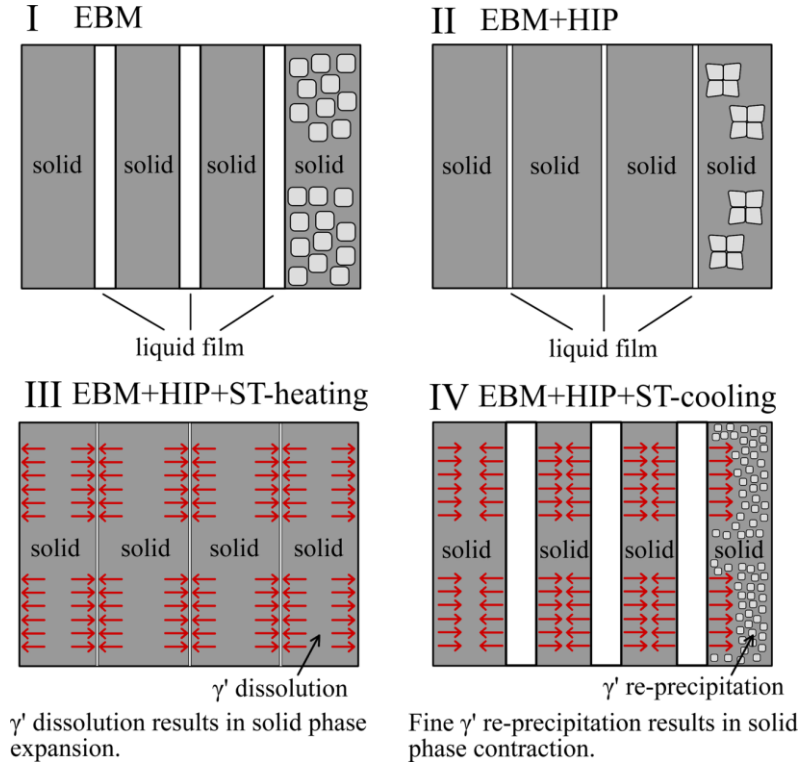

Fig. 17 A schematic diagram showing the crack reappearance process due to the solution treating.

Based on the design-of-experiment study, the mechanism responsible for the post-processing induced cracks is proposed with a schematic diagram in Fig. 17. At step I, the presence of EBM induced intergranular cracks are related to the liquid film, as described previously in section 4.3.1. During the HIP process (step II), the applied hydrostatic pressure (150 MPa at 1230 °C) helps to compress the cracked surfaces,

instead of completely healing the cracks, as evidenced in Figs. 15 (c) and (d). The cooling step after the HIP usually involves a gradual removal of hydrostatic pressure, hence it does not favour the crack surface re-opening. While the HIPped sample is heated to and held at 1230 °C, the solid phase expands due to γ' dissolution, thus creating compressive stresses to the cracked surfaces (step III). The most detrimental step is the cooling stage after solution treating (step IV), where the presence of γ' re-precipitation leads to the ageing contraction effect, thus creating tensile stresses to the cracked surfaces. As a result, a higher number of intergranular cracks with greater crack opening width were observed in the EBM+HIP+STA samples.

5. Conclusions

The following conclusions can be drawn from the results:

1) Both the columnar and near-equiaxed grain structures can be obtained by EBM. There is a need to perform a solution treating and ageing post-processing to promote a more uniformly distributed and more cuboidal shaped γ' precipitates, as such γ' morphology cannot be obtained in as-EBM condition.
2) The columnar grain width in the as-EBM sample exhibited moderate increase from the bottom to the top. By using an appropriate build temperature, i.e. below γ' ageing temperature, the unwanted size gradient in γ' from the bottom to the top can be avoided.
3) Both the room temperature and 850 ºC tensile properties of EBM-built DZ125 in HIP condition have been found to be comparable to cast+STA condition.
4) EBM induced cracks are classified as liquid-state cracking. These cracks were found exclusively at columnar grain boundaries for both CCG and FCG as-EBM samples.
5) Reappearance of intergranular cracks with a much wider crack opening width was observed in the EBM+HIP+STA condition. The post-processing induced cracks can be attributed to the effect of γ' dissolution and re-precipitation of fine γ' during the cooling stage of solution treating.

By clarifying the underlying mechanism for crack formation in both the EBM and post-processed samples, it is suggested that HIP is not an effective approach in healing liquid-state cracks in EBM fabricated γ' precipitation-strengthened superalloys.

In this case, the HIP is most likely a pitfall, i.e. the EBM induced cracks are pretended to be healed under the hydrostatic pressure.

Acknowledgements

BC acknowledges financial supports by Coventry University through the Early Career Researcher – Outgoing Mobility Award, Beihang University in China through the Visiting Associate Professorship, and the UK's Engineering and Physical Sciences Research Council, EPSRC (EP/P025978/1), for facilitating this research collaboration. HP and BC are grateful to Prof. Zihua Zhao, Beihang University, for providing access to HIP facility, and Mr Huankun Li, Beihang University, for support in operating the EBM machine.

References

[1] L.M. Roncery, I. Lopez-Galilea, B. Ruttert, S. Huth, W. Theisen, *Mater. Des.*, 2016, vol. 97, pp. 544-552.
[2] J.N. DuPont, C.V. Robino, A.R. Marder, M.R. Notis, J.R. Michael, *Metall. Mater. Trans. A*, 1988, vol. 29, pp. 2785-2796.
[3] P.S. Kotval, J.D. Venables, R.W. Calder, *Metall. Mater. Trans. B*, 1972, vol. 3, pp. 457-462.
[4] J.E. Doherty, B.H. Kea, A.F. Giamei, *JOM*, 1971, vol. 23, pp. 59-62.
[5] S.C. Deevi, V.K. Sikka, C.T. Liu, *Prog. Mater. Sci.*, 1997, vol. 42, pp. 177-192.
[6] C. Korner, *Int. Mater. Rev.*, 2016, vol. 61, pp. 361-377.
[7] H.E. Helmer, A. BauereiB, R.F. Singer, C. Korner, *Mater. Sci. Eng. A*, 2016, vol. 668, pp. 180-187.
[8] N. Raghavan, R. Dehoff, S. Pannala, S. Simunovic, M. Kirka, J. Turner, N. Carlson, S.S. Babu, *Acta Mater.*, 2016, vol. 112, pp. 303-314.
[9] N. Hrabe, T. Quinn, *Mater. Sci. Eng. A*, 2013, vol. 573, pp. 264-270.
[10] L.E. Murr, E.V. Esquivel, S.A. Quinones, S.M. Gaytan, M.I. Lopez, E.Y. Martinez, F.R. Medina, J. Hernandez, D.A. Ramirez, E. Martinez, J.L. Martinez, S.W. Stafford, D.K. Brown, T. Hoppe, W. Meyers, U. Lindhe, R.B. Wicker, *Mater. Charact.*, 2009, vol. 60, pp. 96-105.
[11] M. Probstle, S. Neumeier, J. Hopfenmuller, L.P. Freund, T. Niendorf, D. Schwarze, M. Goken, *Mater. Sci. Eng. A*, 2016, vol. 674, pp. 299-307.
[12] X. Wang, L.N. Carter, B. Pang, M.M. Attallah, M.H. Loretto, *Acta Mater.*, 2017, vol. 128, pp. 87-95.
[13] L.E. Murr, E. Martinez, X.M. Pan, S.M. Gaytan, J.A. Castrob, C.A. Terrazas, F. Medina, R.B. Wicker, D.H. Abbott, *Acta Mater.*, 2013, vol. 61, pp. 4289-4296.
[14] A. Strondl, M. Palm, J. Gnauk, G. Frommeyer, *Mater. Sci. Tech.*, 2011, vol. 27, pp. 876-883.
[15] J.N. DuPont, J.C. Lippold, S.D. Kiser, Welding Metallurgy and Weldability of Nickel-base Alloys, Wiley, New Jersey, 2009.
[16] A. Strondl, R. Fischer, G. Frommeyer, A. Schneider, *Mater. Sci. Eng. A*, 2008, vol. 480, pp. 138-147.
[17] M.M. Kirka, F. Medina, R. Dehoff, A. Okello, *Mater. Sci. Eng. A*, 2017, vol. 680, pp. 338-346.
[18] M.E. Aydinoz, F. Brenne, M. Schaper, C. Schaak, W. Tillmann, J. Nellesen, T. Niendorf, *Mater. Sci. Eng. A*, 2016, vol. 669, pp. 246-258.
[19] W. Tillmann, C. Schaak, J. Nellesen, M. Schaper, M.E. Aydinoz, K.P. Hoyer, *Addit. Manufact.*, 2017, vol. 13, pp. 93-102.
[20] L.N. Carter, C. Martin, P.J. Withers, M.M. Attallah, *J. Alloy Compd.*, 2014, vol. 615, pp. 338-347.
[21] M. Cloots, P.J. Uggowitzer, K. Wegener, *Mater. Des.*, 2016, vol. 89, pp. 770-784.

[22] N.J. Harrison, I. Todd, K. Mumtaz, *Acta Mater.*, 2015, vol. 94, pp. 59-68.
[23] M. Ramsperger, R.F. Singer, C. Korner, *Metall. Mater. Trans. A*, 2016, vol. 47, pp. 1469-1480.
[24] B. Ruttert, M. Ramsperger, L. Mujica Roncery, I. Lopez-Galilea, C. Korner, W. Theisen, *Mater. Des.*, 2016, vol. 110, pp. 720-727.
[25] E. Chauvet, P. Kontis, E.A. Jagle, B. Gault, D. Raabe, C. Tassin, J. Blandin, R. Dendievel, B. Vayre, S. Abed, G. Martin, *Acta Mater.*, 2018, vol. 142, pp. 82-94.
[26] H. Sun, S. Tian, N. Tian, H. Yu, X. Meng, *Prog. Nat. Sci. Mater. Int.*, 2014, vol. 24, pp. 266-273.
[27] M. Ramsperger, L.M. Roncery, I. Lopez-Galilea, R.F. Singer, W. Theisen, C. Korner, *Adv. Eng. Mater.*, 2015, vol. 17, pp. 1486-1493.
[28] E.W. Ross, K.S. O'Hara, Rene' 142: A high strength, oxidation resistance DS turbine airfoil alloy, in: S.D. Antolovich (Ed.) Superalloys 1992: 7th International Symposium on Superalloys, TMS (The Minerals, Metals & Materials Society), John Wiley & Sons, Inc., Champion, PA, 1992.
[29] E112-13 - Standard Test Methods for Determining Average Grain Size, ASTM International.
[30] J. Zhang, R.F. Singer, *Acta Mater.*, 2002, vol. 50, pp. 1869-1879.
[31] N. Wang, S. Mokadem, M. Rappaz, W. Kurz, *Acta Mater.*, 2004, vol. 52, pp. 3173-3182.
[32] R.A. Ricks, A.J. Porter, R.C. Ecob, *Acta Metall.*, 1983, vol. 31, pp. 43-53.
[33] J. Zhang, R.F. Singer, *Metall. Mater. Trans. A*, 2004, vol. 35, pp. 939-946.
[34] X. Tan, Y. Kok, Y.J. Tan, M. Descoins, D. Mangelinck, S.B. Tor, K.F. Leong, C.K. Chua, *Acta Mater.*, 2015, vol. 97, pp. 1-16.
[35] R.C. Reed, The Superalloys Fundamentals and Applications, Cambridge University Press, Cambridge, 2006.
[36] L.N. Carter, M.M. Attallah, R.C. Reed, Laser powder bed fabrication of nickel-base superalloys: influence of parameters; characterization, quantification and mitigation of cracking, in: E.S. Huron, R.C. Reed, M.C. Hardy, M.J. Mills, R.E. Montero, P.D. Portella, J. Telesman (Eds.) Superalloys 2012: 12th International Symposium on Superalloys, TMS (The Minerals, Metals & Materials Society), John Wiley & Sons, Inc., Pennsylvania, 2012.
[37] M. Zhong, H. Sun, W. Liu, X. Zhu, J. He, *Scripta Mater.*, 2005, vol. 53, pp. 159-164.
[38] D. Dye, O. Hunziker, R.C. Reed, *Acta Mater.*, 2001, vol. 49, pp. 683-697.
[39] A.J. Ramirez, J.C. Lippold, *Mater. Sci. Eng. A*, 2004, vol. 380, pp. 245-258.
[40] S. Kou, *JOM*, 2003, vol. 55, pp. 37-42.
[41] J.E. Franklin, W.F. Savage, *Weld. J.*, 1974, vol. 53, pp. 380s-387s.

List of Figure Captions

Figure 1 Schematic diagrams of (a) one batch of as-EBM DZ125 samples; (b) electron beam scans in a snake-like way with a specific L_{off} and the hatching direction is changed by 90° after each build layer of 50 μm; (c) the EBM sample position where metallographic specimens were extracted for microstructural evaluations. Note: the indicated (c) in Fig. 1(a) represents the microstructural characterisation region as shown in Fig. 1(c).

Figure 2 SEM micrographs and particle size distribution of pre-alloyed DZ125 powders: (a) the powder morphology, (b) a single ground and polished powder particle showing microdendritic structure, and (c) volume fraction distribution and cumulative volume fraction of powder particles.

Figure 3 Optical micrographs in the X-Z plane of DZ125 samples fabricated by EBM with different E_A values: (a) sample 1 with E_A=1.88 J/mm^2; (b) sample 2 with E_A=2.07 J/mm^2; (c) sample 3(CCG) with E_A=2.31 J/mm^2; (d) sample 4(FCG) with E_A=2.50 J/mm^2; (e) sample 5 with E_A=2.50 J/mm^2; (f) sample 6 with E_A=5.00 J/mm^2. Note: Numbers correspond to samples IDs given in Table 1.

Figure 4 EBSD γ-phase IPF orientation maps of DZ125 samples fabricated by EBM with different E_A values: (a) sample 1 with E_A=1.88 J/mm^2; (b) sample 2 with E_A=2.07 J/mm^2; (c) sample 3(CCG) with E_A=2.31 J/mm^2; (d) sample 4(FCG) with E_A=2.50 J/mm^2; (e) sample 5 with E_A=2.50 J/mm^2; (f) sample 6 with E_A=5.00 J/mm^2.

Figure 5 SEM micrographs of as-EBM DZ125 sample 3(CCG) with a typical columnar grain structure: (a) low magnification SEM image showing different columnar grains as indicated from A to D; (b) high magnification SEM image showing dendrite core and dendrite boundary regions within the columnar grain C; (c) and (d) enlarged SEM images showing the presence of larger sized γ′ phase at dendrite boundary region.

Figure 6 (a) SEM micrograph in the X-Z plane of as-EBM sample 3(CCG) showing that MC carbides nucleate preferably at the columnar grain boundary and dendrite boundary regions; (b) a schematic diagram delineating the locations of MC carbides.

Figure 7 Optical micrographs of cast DZ125: (a) as-cast and (b) cast+STA.

Figure 8 SEM micrographs of as-EBM samples 3 and 4 as well as cast DZ125 samples showing the morphology of γ′ precipitates: (a) as-EBM sample 3 (CCG); (b) as-EBM sample 4 (FCG); (c) as-cast sample; (d) cast+STA sample.

Figure 9 Measured average size of γ′ precipitates of as-EBM samples 3 and 4 and their changes due to HIP and STA heat treatment. These are compared with the cast DZ125 in both as-cast and cast+STA conditions. The γ′ precipitates at dendrite core and dendrite boundary location are considered separately for the as-EBM condition.

Figure 10 SEM micrographs of γ′ phase in the X-Z plane of EBM-built DZ125 alloys: (a) and (b) EBM+HIP condition for samples 3 (CCG) and 4 (FCG); (c) and (d) EBM+HIP+STA condition for samples 3 (CCG) and 4 (FCG).

Figure 11 Crack morphology of as-EBM DZ125: (a) and (b) optical micrographs of samples 3 (CCG) and 4 (FCG) showing the cracks along the columnar grain boundaries; (c) and (d) SEM micrograph of samples 3 and 4 showing the distribution of MC carbides close to the cracked grain boundary region and dendrite boundaries.

Figure 12 SEM and optical micrographs showing reappearance of intergranular cracks due to the post-processing: (a) and (b) samples 3 and 4 in HIP condition; (c) and (d) samples 3 and 4 in HIP+STA condition. Upper two figures in (c) and (d) are optical micrographs of polished specimens and the lower two figures are SEM micrographs of etched specimens.

Figure 13 Optical and SEM micrographs of sample 4: (a) 1280°C HIP condition showing that EBM induced cracks can be fully closely with an increasing HIP temperature; (b) 1280°C HIP+STA condition showing the reappearance of intergranular cracks; (c) and (d) γ′ precipitates morphological evolution as a result of 1280°C HIP and STA treatment.

Figure 14 (a) Room temperature Vickers hardness measurements on EBM-built samples 3 and 4 as well as cast DZ125; (b) Monotonic tensile tests at 850 °C on samples 3 and 4 in HIP condition as well as cast DZ125 sample in STA condition.

Figure 15 SEM fractography examination of the cracked surfaces: (a) as-EBM sample 3; (b) as-EBM sample 4; (c) EBM+HIP sample 3; (d) EBM+HIP sample 4; (e) EBM+HIP+STA sample 3 and (f) EBM+HIP+STA sample 4

Figure 16 SEM micrographs of γ′ precipitates evolution and cracking in sample 3 with the initial condition of EBM+HIP: (a) heat to 1230 °C and hold for 1 h, finally cooled to room temperature; (b) heat to 1230 °C and hold for 3 h, finally cooled to room temperature; (c) and (d) observed intergranular cracks for each condition by optical microscopy.

Figure 17 A schematic diagram showing the crack reappearance process due to the solution treating.

Table 1 EBM processing parameters [v: scanning speed; L_{off}: line offset; P: beam power; $E_A=P/(v\times L_{off})$: area energy] and the measured columnar grain width as well as grain aspect ratio for each as-EBM sample. Note: Samples 3 and 4 are also named as CCG (coarse columnar grain structure) and FCG (fine columnar grain structure).

Sample ID	v (mm/s)	L_{off} (mm)	P (W)	E_A (J/mm^2)	Grain width (μm)	Grain aspect ratio
1	3200	0.10	600	1.88	149.6±21.7	13.1±3.1
2	2900	0.10		2.07	581.9±50.3	N/A (>10 mm for grain length)
3 (CCG)	2600	0.10		2.31	709.5±64.7	
4 (FCG)	800	0.15	300	2.50	170.0±24.3	26.8±5.7
5	1200	0.10		2.50	87.5±13.5	18.8±4.0
6	3000	0.02		5.00	32.1±11.5	3.4±0.5

Table 2 Nominal composition of PREP DZ125 powder (in wt%).

C	Cr	Co	Mo	W	Ta	Ti	Al	B	Hf	Ni
0.078	9.17	9.74	2.14	6.73	3.61	1.04	5.05	0.014	1.51	Bal.

Table 3 EDS analysis of precipitates in as-EBM sample 5(CCG) (wt%)

Location	Al	Ta	Mo	Cr	Co	Ni	Hf
γ/γ′	4.96	7.73	2.89	12.20	11.73	58.64	1.70
MC carbide	1.59	26.18	2.01	5.10	5.06	21.79	38.03

Table 4 Summary of the γ' precipitate size and its volume fraction, γ channel width and crack ratios for as-EBM and post-processed samples 3 and 4 and the reference cast DZ125. Note: there was little difference in measured γ' size at dendrite core and dendrite boundary in specimens that had been subjected to HIP and STA heat treatment.

Sample ID	Condition	γ channel width (μm)	Average γ' size (μm)	γ' (vol%)	Crack ratio (%)
Sample 3 (CCG)	EBM	0.06±0.02	0.31±0.04 (core) 0.45±0.11 (boundary)	64	2.60
	EBM+HIP	0.19±0.06	1.31±0.08	67	1.29
	EBM+HIP+STA	0.06±0.01	0.64±0.05	76	5.69
Sample 4 (FCG)	EBM	0.05±0.02	0.33±0.06 (core) 0.47±0.09 (boundary)	70	2.72
	EBM+HIP	0.20±0.08	1.26±0.09	64	1.03
	EBM+HIP+STA	0.07±0.02	0.69±0.07	75	4.93
Cast DZ125	As-cast	0.09±0.04	0.61±0.07	66	N/A
	Cast+STA	0.05±0.01	0.54±0.03	77	N/A

Table 5 Summary of columnar grain width, γ' size and volume fraction as a function of build height positions for specimen 3 in as-EBM condition

Z, mm	Grain width (μm)	Average γ' size (μm)		γ' (vol%)	Vickers Hardness
		core	boundary		
10	542.6±17.2	0.40±0.06	0.47±0.15	57	457.4±7.8
30	593.8±20.7	0.42±0.06	0.47±0.14	64	473.4±10.6
50	700.0±18.9	0.39±0.07	0.46±0.15	64	468.0±10.0
70	886.5±19.3	0.35±0.05	0.44±0.16	67	470.3±20.4